Analysis of the THz Responsivity of AlGaN/GaN HEMTs by means of Monte Carlo Simulations

Sergio García-Sánchez, Ignacio Íñiguez-de-la-Torre, Gaudencio Paz-Martínez, Philippe Artillan, Tomás González, *Senior Member, IEEE*, and Javier Mateos, *Member, IEEE*

***Abstract*—In this work, by means of Monte Carlo (MC) simulations, the current responsivity of AlGaN/GaN HEMTs operating as zero-bias detectors is analyzed, reaching the THz frequency range. Two approaches are used for the calculation of the responsivity, trying to get physical information on the detection mechanisms from the comparison of their respective results. First, we determine the responsivity directly from the MC values of DC drain current shift originated by an input AC drain voltage excitation. As second approach, the responsivity is estimated from a closed-form expression involving the MC calculation of both the DC I-V curves of the transistor (to determine Taylor expansion coefficients) and the AC response in terms of the Y-parameters (to be converted into S-parameters). Both approaches coincide at low frequency, but the closed-form expression starts to deviate from the correct result at frequencies around 1 THz. Moreover, a modest plasma resonance is visible in the 2-5 THz range.**

***Index Terms*—Monte Carlo Simulations, Analytical model, High-electron mobility transistor (HEMT), GaN, Microwave detector, Power detector, Terahertz (THz) detectors, Responsivity model**

I. INTRODUCTION

THE field of Terahertz science and technology is gaining international interest due to its broad potential applications, ranging from ultra-high speed wireless communication systems to sensing and imaging for medical diagnostic, industrial quality control, security-screening tools, THz astronomy or pharmacology. As described in the detailed snapshot of the 2017 state-of-the-art THz technologies made in Ref. [1] photonic and electronic approaches compete for conquering the "THz gap" but optical approaches often need for bulky and expensive equipment. Detectors based on different technologies (bolometers, pyroelectric detectors, Golay cells, Josephson junctions, etc.) are available [2], [3], but due to its simplicity, compactness and speed of response, Schottky barrier diodes (SBDs) are presently the benchmarking reference for THz detection [4], even if their sensitivity is not the best (with values of Noise Equivalent Power, NEP, around $250\,\mathrm{pW}/\sqrt{\mathrm{Hz}}$ in the 1.5 THz range, as compared with the tens of $\mathrm{pW}/\sqrt{\mathrm{Hz}}$ provided by bolometers). However, the large value of its input impedance when using them as zero-bias detectors poses significant complications for their design, so that other approaches, such as 3-terminal Field-Effect Transistors (FETs), are being explored in the recent years. In fact, apart from their "classical" operation as amplifiers and digital switches, they have demonstrated to provide good performances as THz detectors well above their typical cut-off frequencies f_t and f_{max}. This is coherent with the fact that, by definition, those cut-off frequencies indicate the limit of operation of transistors as amplifiers (used as a 2 port circuit) under different loads, while when used as THz detectors, the operating conditions are completely different (as well explained in Refs. [5] and [6]), since they act as a one-port circuit, with just one AC input (RF or THz) and one DC output.

At low frequencies, the physical origin of the detection with FETs is a resistive self-mixing mechanism [7], [8], given by the nonlinearity of the I_d-V_{ds} curves. The frequency dependence can be described using the well-established voltage dependent lumped element modelling by means of a Small-Signal Equivalent Circuit (SSEC). This kind of approach is able to correctly explain the results obtained in graphene FETs up to almost 1 THz [6], and has been helpful for the optimization of the design of the detectors [7]. However, for higher frequencies, the consideration of more complex models is necessary. For example, resonant plasma waves can have a contribution to the detection at THz frequencies, but only to a limited extent (much lower than expected by the Dyakonov–Shur theory) due to the high-frequency dependence of the channel impedance [7], not considered in the ideal plasma-wave models [9]. Another mechanism suggested to be significant at intermediate and high frequencies is the hot-carrier thermoemission process [10], in which thermoelectric emission of electrons above the barrier imposed by the gate potential is able to provide a non-zero drain current, and thus allows for RF detection with FETs. Taking advantage of the better understanding of the FET detection mechanisms and making use of circuit models, the fabrication of THz detectors based on FETs with specific designs (and often with integrated antennae for an improved free-space coupling) have been achieved in the last times [5], [6], [7], [11].

However, a clear understanding of the detection mechanisms in FETs in the whole frequency range is still lacking. Monte Carlo (MC) simulations, containing all the ingredients to tackle

Manuscript received XX Month 2024. This work has been partially supported through grant PID2020-115842RB-I00 funded by MCIN/AEI/10.13039/501100011033 and the Junta de Castilla y León and FEDER through project SA136P23. This research has made use of the high performance computing resources of the Castilla y León Supercomputing Center (SCAYLE, www.scayle.es), financed by the European Regional Development Fund (ERDF). (*Corresponding author: Sergio García-Sánchez*)

S. García-Sánchez, I. Íñiguez-de-la-Torre, G. Paz-Martínez, T. González and J. Mateos are with with the Applied Physics Department, and USAL-NANOLAB, Universidad de Salamanca, 37008 Salamanca, Spain (e-mail: sergio_gs@usal.es, indy@usal.es, gaupaz@usal.es, tomasg@usal.es and javierm@usal.es).

P. Artillan is with Univ. Grenoble Alpes, Univ. Savoie Mont Blanc, CNRS, Grenoble INP, IMEP-LAHC, 38000 Grenoble, France (e-mail: philippe.artillan@univ-smb.fr).

this problem, have been scarcely exploited so far; only a first attempt to qualitatively study the THz rectification capabilities of InGaAs HEMTs was made by some of the authors in Ref. [12]. In this paper, by means of detailed MC simulations, we will provide a physics-based description of the detection with GaN HEMTs, from low frequency (several GHz) to the THz range, thus allowing to determine up to which frequency the resistive-mixing concept is valid and to which extent the celebrated resonant plasma-wave (together with hot-carrier thermoemission process) enhancement of THz detection is feasible with present technologies. We will make use of the closed-form model developed in Ref. [13] for the case of resistive-mixing detection in order to identify the contribution of this specific detection mechanism. In this way we will be able to compare results on ideal models of a same device simulated in transient and harmonic representation, without focusing on the fitting of experimental results and avoiding discrepancies associated with experimental errors or electrical models used in the measurements.

The organization of this paper is as follows: firstly, the information about the MC simulator and the details of the device under test are provided. Following this, it delves into the description and comparison of the two approaches used for the calculation of the AC responsivity, a direct MC simulation and a closed-form expression based on the I_d-V_{ds} curves and the values of the S-parameters of the device. Finally, the paper summarizes the main conclusions drawn from the analysis.

II. Monte Carlo Simulator and device details

For the simulation, we will use a two-dimensional (2D) semi-classical ensemble MC model self-consistently coupled with the solution of the Poisson equation [14]. The microscopic dynamics of the electron transport is simulated in time steps of Δt=1.0 fs, where free flights are truncated by scattering mechanisms (considered instantaneous) which change the trajectory and energy of electrons. The scattering mechanisms included in the simulator are: intervalley, acoustic and optical (polar and non-polar) phonons and piezoelectric [15], [16]. At the end of each time step Δt, the Poisson equation is solved using a mesh size ranging between 0.5 and 5 nm (depending on the electron concentration level), providing the electric field to be taken into account in the next time step in each cell. The Poisson solver makes use of the LU decomposition algorithm [17] in a finite differences approach suitable for non uniform meshes and complicated geometries. In order to correctly take into account the quantum behaviour of the electrons within the 2DEG it would be necessary to solve the Schrödinger equation self-consistently with Poisson equation, and then calculate the sub-bands energy levels and the 2D scattering rates for electrons. The electron confinement also gives rise to other quantum effects such as degeneracy and tunneling from the channel to the gate. However, in order to keep the calculation time at an acceptable level we will make use of a semiclassical MC model which locally takes into account the effect of the degeneracy by using the rejection technique [18], and the rest of quantum effects are not considered. This assumption does not introduce a significant error at room temperature.

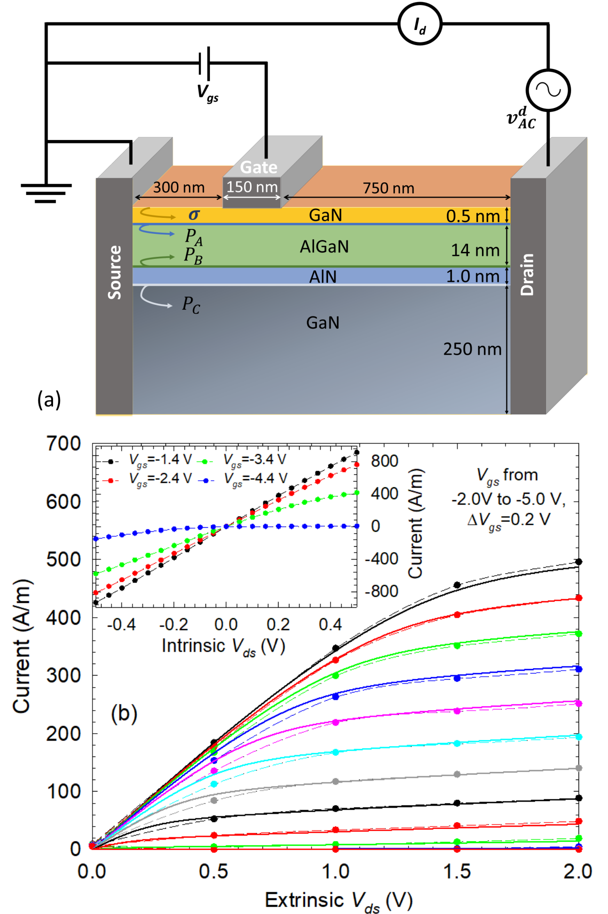

Fig. 1. (a) Sketch of the simulated 150-nm gate GaN HEMT (and the setup for DI detection simulations) and (b) comparison of its experimental I_d-V_{ds} output characteristics (solid lines) and those obtained with MC simulations (circles, dashed lines). The values used for the source and drain contact resistances are R_s=1.6 Ω·mm, R_d=0.3 Ω·mm, respectively (in good agreement with the measured data) and 0.65 eV for the Schottky barrier height at the gate metal-semiconductor junction. The inset in (b) shows the intrinsic simulated curves in the low V_{ds} bias region, where the simulations of the detection are performed.

Ohmic boundary conditions (following the model presented in Ref. [19]) are considered in the source and drain contacts, which are simulated in vertical position, adjacent to the different material layers. Accordingly, nonuniform potential and concentration profiles are considered along these contacts: those that would be obtained if real top electrodes were simulated [20], [21]. These profiles are calculated from a separated simulation at equilibrium and are applied for every biasing. The Schottky gate is simulated as a non-injecting, perfectly absorbing contact. The conduction band of GaN (Wurtzite crystal structure), AlGaN and AlN are modelled by three non-parabolic spherical valleys (Γ_1, U and Γ_3). The classical laws of conservation of total energy and momentum perpendicular to the heterojunctions are used for modelling the electron transfer at the heterolayers. If the normal energy is enough to jump over the barrier, the carrier has a transmission coefficient of 1, in other case it is specularly reflected; quantum reflection and tunneling are not considered. In this kind of processes it is assumed that the electron does not change

of valley, since the important variation of momentum which implies an intervalley transition makes it highly improbable. The conduction band discontinuities imposed at the AlN/GaN, AlGaN/AlN, and GaN/AlGaN heterojunctions are, 1.57 eV, 1.1 eV and 0.47 eV, respectively. More details about the model and the parameters used in the MC simulations can be found in Refs. [15], [22], [23].

The topology of simulation domain, depicted in Fig. 1(a), reproduces that of the real device as closely as possible. However, in order to optimize the computation time the source and drain contacts are simulated as vertical interfaces with adequate injection and potential profiles [24], [25], and the simulated source-gate region has been reduced to 300 nm instead of 600 nm (it is just an ohmic region, whose influence can be analytically included in a post-processing stage). The mesh to solve the Poisson equation consists of 56 rows and 240 columns, having a total number of 13,440 cells. Finally, in order to reproduce electron mobility in the channel (1800 $cm^2V^{-1}s^{-1}$), dislocation and roughness scattering at the AlGaN/GaN heterointerface have also been considered [16], [26].

The GaN HEMT studied in this paper is based on a AlGaN/GaN heterostructure with a 14 nm thick $Al_{0.29}GaN_{0.71}$ layer, a 1.0 nm AlN spacer and a 0.5 nm GaN cap, the same used in [16], [27], whose fabrication was explained in [16], [28]. The material parameters used in the simulation of the GaN cap are the same as those used for the channel, even if some deviation is expected due to its small thickness. In any case this layer is completely depleted, so that its influence is not significant. The C-doping used in the bottom GaN layer in order to provide a better confinement of electrons near the heterojunction [27] has been included in the simulations by considering a p-type doping with N_A=10^{17} cm^{-3}. To ensure an accurate simulation of such epitaxial structure, we add surface charges reproducing the effect of spontaneous and piezoelectric polarization at every heterojunction [29], [30], [31], denoted as P_A, P_B and P_C (located at the GaN/AlGaN, AlGaN/AlN and AlN/GaN heterojunctions with values of -2, -2 and 15×10^{12} cm^{-2}, respectively, see Fig. 1(a)). Additionally, a surface charge density σ=-1×10^{12} cm^{-2} is added at the top of the cap GaN layer. As a consequence, the charge-neutrality condition at equilibrium P_A+P_B+P_C+σ-n_s=0 provides the experimental value for the electron sheet charge density in the 2DEG n_s=10^{13} cm^{-2}.

MC simulations of the intrinsic device shown in Fig. 1(a) are able to very closely reproduce the extrinsic I_d-V_{ds} curves of a real 150 nm-gate GaN HEMT with 2×25 μm width, Fig. 1(b), by analytically including the effect of the extrinsic resistances and the Schottky barrier height [32]. In the following we will present the results of the simulations of the intrinsic device (the inset of Fig. 1(b) shows the intrinsic I_d-V_{ds} curves), since the effect of the parasitic resistances and capacitances, which are quite significant, should be studied separately.

III. Results and Discussion

A. AC Power Detection: Direct Monte Carlo Simulations

Time-domain MC simulations allow to directly reproduce the AC power detection experiments by applying a sinusoidal voltage signal with frequency f to the gate or drain terminals (leading to gate-injection, GI, or drain-injection, DI, modes, respectively) and taking the short-circuited drain current as output signal. This zero-bias detection conditions (in absence of drain bias) are the optimum ones for improving the low-noise operation of the detectors, and therefore their sensitivity, due to the suppression of the low frequency (mainly $1/f$) noise appearing when the drain is biased. In this paper we will focus on DI in order to avoid the low-frequency dependence displayed by the GI case [27]. Fig. 1(a) shows a sketch of such simulation scheme.

The responsivity within this DI zero-bias current-mode detection scheme, $\beta_{d,opt}$, is calculated directly using MC simulations by computing the DC average of the drain current, $\overline{i_d}$, when a single tone voltage signal $v^d_{AC}(f)$ with amplitude 0.25 V is applied to the drain terminal, see Fig. 1(a), as:

$$\beta_{d,opt}(f) = \frac{\overline{i_d}(f)}{P_{AC}(f)}, \quad (1)$$

where P_{AC} is the AC power absorbed by the device. P_{AC} is computed within the time domain MC simulation as the average value of the $v_d(t)\times i_d(t)$ product (being $i_d(t)$ the instantaneous drain current provided by the MC simulation).

The previous calculation provides the optimum responsivity of the detector assuming a perfect impedance matching with the AC power source. However, in real-world experiments the impedance of the source, R_0, is significantly lower than that of the transistor (mainly for V_{gs} near pinch-off). As a result, in order to extract the practical value of the responsivity we have to take into account the reflection coefficient at the input port (i. e. the drain, since DI is considered here), $\Gamma_d(f)$. The expression for this mismatched value of the DI responsivity, β_d, is given by:

$$\beta_d(f) = \beta_{d,opt}(f)\left(1 - |\Gamma_d(f)|^2\right) \quad (2)$$

where Γ_d is not just the S_{22} parameter of the transistor, but depends on both the S-parameters of the device and the load connected to the gate terminal [33], since

$$\Gamma_d(f) = \frac{S_{22} - \Delta S\,\Gamma_L}{1 - S_{11}\Gamma_L}, \quad (3)$$

being Γ_L the reflection coefficient of the load, and ΔS=$S_{22}S_{11}$−$S_{21}S_{12}$. In the case when the gate is connected to a R_0 load, Γ_L=0 and simply Γ_d=S_{22}, but for a short-circuited gate (as in MC simulations), Γ_L=-1 and $\Gamma_d \neq S_{22}$. Thus, the direct calculation of the responsivity using MC simulations, β_d^{MC}, is the following:

$$\beta_d^{MC}(f) = \beta_{d,opt}(f)\left(1 - \left|S_{22} - \frac{S_{12}S_{21}}{1 + S_{11}}\right|^2\right) \quad (4)$$

The S-parameters can be obtained from MC simulations (as explained later) using the well-known two-port conversion

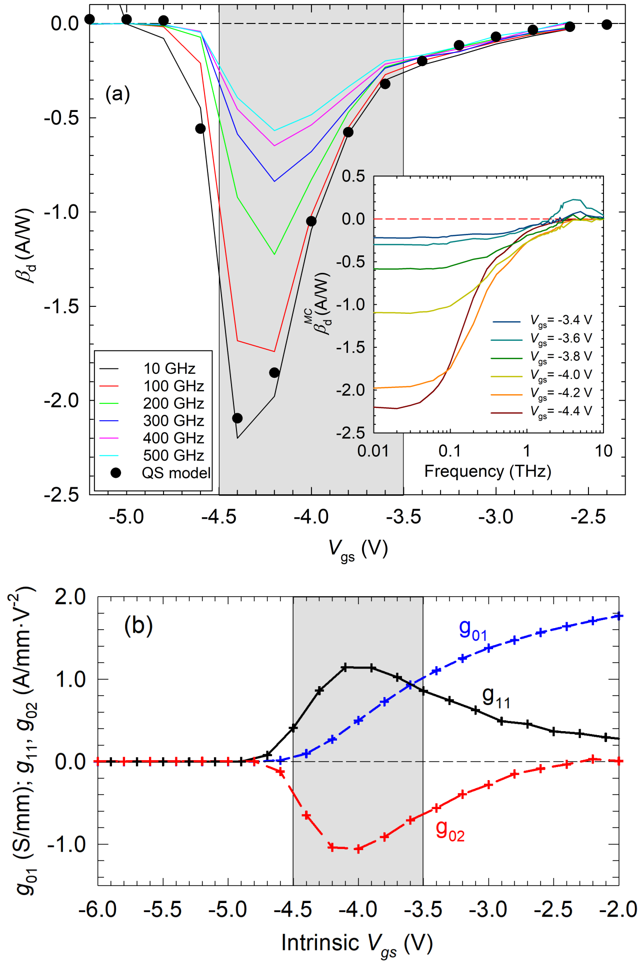

Fig. 2. Current responsivity in (A/W) for different values of the frequency of the drain-injected signal (up to 500 GHz) as a function of V_{gs}. Lines correspond to direct MC simulations of detection, β_d^{MC}, and black dots to the quasi-static prediction. The inset shows the frequency dependence of β_d^{MC} up to 10 THz for different values of V_{gs}. (b) Coefficients g_{01}, g_{02}, and g_{11} obtained from the derivatives of the intrinsic I_d-V_{ds} curves using eq. (5).

equation from Y to S matrix considering a load impedance of R_0=50 Ω [34].

Fig. 2(a) shows the dependencies on frequency and V_{gs} of the simulated responsivity of the GaN HEMT obtained directly from MC simulations by applying eq. (2). As expected, β_d^{MC} shows always negative values with a maximum in V_{gs} (of about -2.3 A/W) located just above the threshold voltage (with an intrinsic value of around $-4.6\,V$), following the behaviour typically obtained in the detection experiments realized with a wide variety of FETs [7], [9], [10], [27], [13]. Using these values of responsivity one can extract the optimum value of the intrinsic NEP, which is around 4.3 pW/$\sqrt{\text{Hz}}$. The intrinsic value of β_d^{MC} obtained with the MC simulations is significantly higher than that obtained in the experiments made with a real device (with maximum values around 1.5 A/W, see [27]), while that of the intrinsic NEP is only slightly lower (minimum of 4.5 pW/$\sqrt{\text{Hz}}$). This happens because the extrinsic contact resistances lead to a significant decrease of the device nonlinearity, which is in part counteracted by a larger resistance (thus providing a lower noise power).

From now on we will focus on the V_{gs} range where maximum responsivity is achieved, between -4.5 and -3.5 V, the gray shaded region in Figs. 2(a) and (b). The frequency dependence of β_d^{MC}, shown in the inset of Fig. 2(a), displays a low-frequency plateau up to around 100 GHz followed by steep roll-off, regardless of the gate bias. At THz frequencies a sign change, with a relatively significant peak at around 4-5 THz (visible mainly at intermediate values of V_{gs}) may indicate the presence of a plasma resonance [12].

B. AC Power Detection: Analytic Formalism Based on I_d-V_{ds} Curves and S-parameters

If one defines the Taylor coefficients, g_{ij}, of the I_d-V_{ds} curves as:

$$g_{ij} = \frac{\partial^{(i+j)} I_d}{\partial^i V_{gs} \partial^j V_{ds}}, \tag{5}$$

whose values are shown in Fig. 2(b), one can easily obtain the expected value for β_d at low frequency [27] using eq. (2) and knowing that $\beta_{d,opt}^{i}(0) \approx g_{02}/2g_{01}$, and using $\Gamma_d(0)$=(R-R_0)/(R+R_0), being R the resistance of the device (note that g_{01}=g_d=1/R, with g_d the drain dynamic conductance). As observed in Fig. 2(a), the prediction of such simple quasi-static (QS) model for the detection based on the nonlinearity of the I_d-V_{ds} curves perfectly agrees with the low frequency value of β_d obtained directly with the time-domain MC simulations.

In order to generalize the previously used quasi-static model for AC power detection and analytically obtain the frequency dependent value of $\beta_d(f)$, we have recently developed (see Ref. [13]) a formalism which provides its value taking as a base the second order Taylor coefficients, g_{ij} (assumed to be frequency independent), where the frequency dependence is included by means of the two-port $S_{ij}(f)$ parameters. The closed-form (CF) expression for the DI current responsivity $\beta_d^{CF}(f)$ in A/W is given by:

$$\beta_d^{CF}(f) = \frac{R_0}{2}\Big(g_{20}|S_{12}(f)|^2 + \overbrace{g_{02}|1+S_{22}(f)|^2}^{\beta_{DD}(f)} \\ \underbrace{+\,2g_{11}\Re\Big[S_{12}^*(f)[1+S_{22}(f)]\Big]}_{\beta_{DG}(f)}\Big). \tag{6}$$

being R_0 the characteristic impedance of the transmission line, typically 50 Ω. This CF expression for the responsivity was obtained in [13] assuming that both drain and gate ports are connected to R_0 loads, as happens in the experiments. However, if the gate is connected to a different load, the S-parameters to be included in the CF expression are those corresponding to the association of the device with its termination (S'-matrix) [33].

The first term in eq. (6) is null, because g_{20}=0 for zero-biased drain (since $\forall V_{gs}, I_d(V_{gs}, V_{ds}{=}0) \approx 0$), so that it can be discarded. The third contribution to $\beta_d^{CF}(f)$, proportional to g_{11}, β_{DG}, is associated to the gate-drain coupling and therefore is null at f=0, so that the QS case explained before is recovered, since, regardless of the value of Γ_L, S_{12}=S_{21}=0 for a FET at low frequency, and the equality $R_0[1{+}\Gamma_d(0)]^2$=$R[1{-}\Gamma_d(0)^2]$ holds [13]. Indeed, the QS

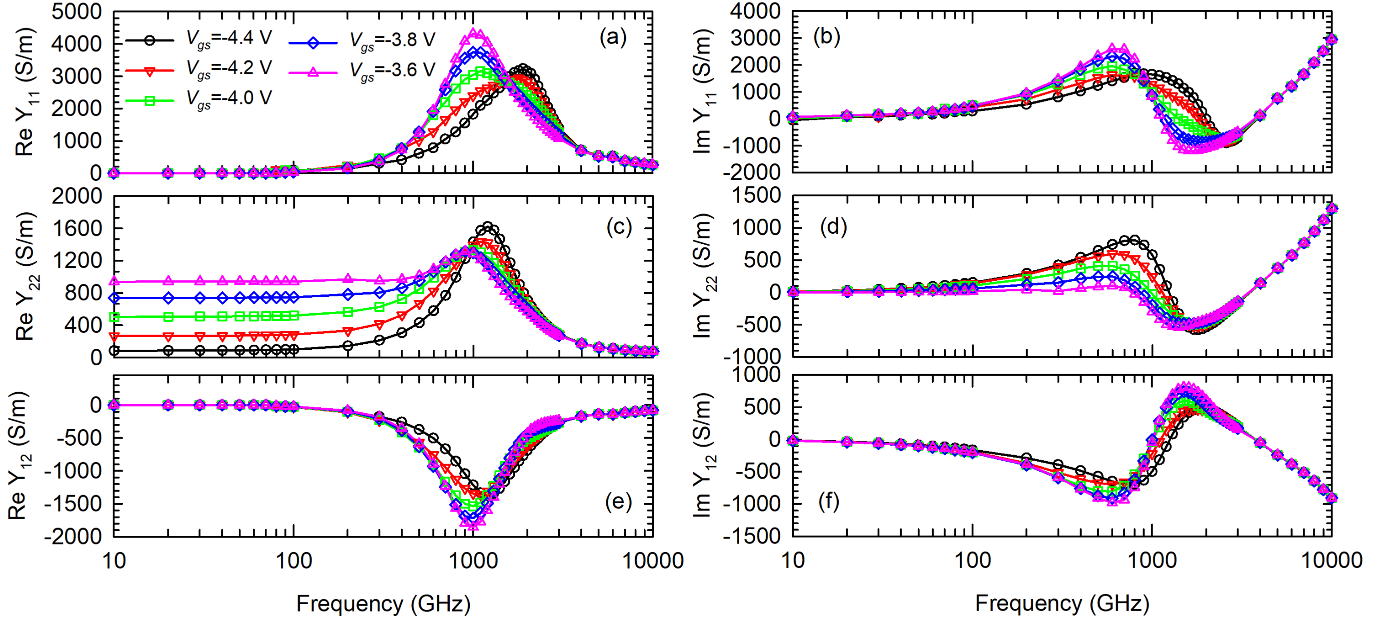

Fig. 3. Real and imaginary parts of the Y_{ij} parameters as a function of frequency computed with MC simulations for different values of V_{gs}=-4.4, -4.2, -4.0, -3.8 and -3.6 V.

model is just a particular case of this general frequency-dependent formalism.

The frequency dependent S-parameter matrix of the device to be included in eqs. (4) and (6) can be straightforwardly obtained from MC simulations by computing its complex Y-parameters, Y_{ij}, defined as:

$$\begin{aligned}\tilde{i}_1 &= Y_{11}\tilde{v}_1 + Y_{12}\tilde{v}_2 \\ \tilde{i}_2 &= Y_{21}\tilde{v}_1 + Y_{22}\tilde{v}_2\end{aligned} \tag{7}$$

being $\tilde{i}_1$ and $\tilde{i}_2$ ($\tilde{v}_1$ and $\tilde{v}_2$) the gate and drain complex representation of the AC currents (voltages), respectively. This is the natural outcome in the case of MC simulations, where voltage sources are used and the current is the output magnitude. In order to compute the values of $Y_{ij}(f)$, a single-tone voltage signal with varying frequency is first applied to the gate terminal (port 1) and the drain and gate currents are recorded in order to extract the complex values of $Y_{11}(f)$ and $Y_{21}(f)$. The same is done for $Y_{12}(f)$ and $Y_{22}(f)$ by applying an AC voltage to the drain contact. The values of the real and imaginary parts of $Y_{ij}(f)$ for different values of V_{gs} are shown in Fig. 3 (note that $Y_{21}(f)$=$Y_{12}(f)$ in unbiased-drain conditions, as in any passive network). As expected, at low frequency a purely capacitive value is obtained for the gate admittance Y_{11} (related to the gate-source and gate-drain capacitances, C_{gs} and C_{gd}, respectively), while the drain admittance Y_{22} displays a plateau in the real part (corresponding to g_d=g_{01}). At higher frequencies, above 100 GHz, the capacitive effects are predominant. Finally, at THz frequencies the well known plasma effects [12] are evident, providing resonances in all the Y parameters at around 1-2 THz (leading to a maximum in the real part and a zero-crossing in the imaginary part).

In order to analyze the frequency dependence of the responsivity according to eq. (6), the values of the factors

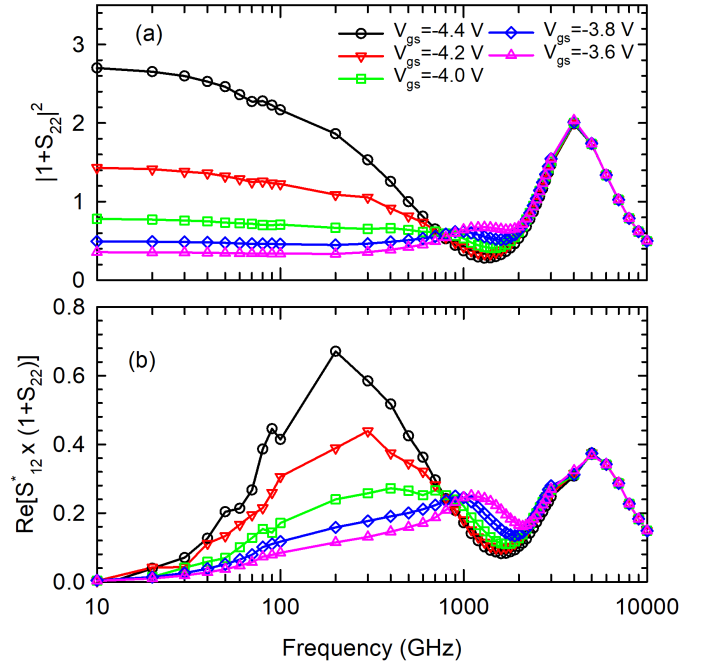

Fig. 4. Frequency dependence of the (a) $DD(f)$=$|1+S_{22}|^2$ and (b) $DG(f)$=$\Re[S_{12}^*(1+S_{22})]$ factors for V_{gs}=-4.4, -4.2, -4.0, -3.8 and -3.6 V.

$DD(f)$=$|1+S_{22}|^2$ and $DG(f)$=$\Re[S_{12}^*(1+S_{22})]$ involved in the formula providing the direct-drain, β_{DD}, and drain-gate coupling, β_{DG}, detection terms (proportional to g_{02} and g_{11}, respectively) are plotted in Fig. 4. The first, $\beta_{DD}(f)$, displays a low-frequency plateau followed by a roll-off starting at frequencies below 100 GHz. On the other hand, $\beta_{DG}(f)$ is null at low frequency and increases in parallel to the decrease of $\beta_{DD}(f)$, peaking at about 200 GHz for low V_{gs}, while

it monotonically increases up to THz frequencies for high V_{gs}. Since g_{02} takes always negative values while g_{11} is positive, both frequency dependencies add up to produce a significant decay in the DI responsivity already evident below 100 GHz, as observed in the symbols of Fig. 5(a). Moreover, since parasitic effects are not considered in these simulations, this cutoff frequency is much higher than that found in the measurements, which is below 10-20 GHz [13].

In Fig. 5(a) we compare the results obtained for $\beta_d^{CF}(f)$ using the analytic expression of eq. (6) (symbols) based on the DC curves and S-parameters of the device and those computed directly with MC simulations (lines) using the averaged DC drain current, $\beta_d^{MC}(f)$ of eq. (4). The first interesting observation is that the low-frequency roll-off is much different due to the fact that MC simulations of the detection do not account for the drain-gate coupling mechanism, as the gate terminal is RF grounded (the electric potential of the gate terminal is fixed to the static value of V_{gs}). As such, the correct quantity to compare with the direct result of the simulations is the value of the CF expression of eq. (6) but using the S'-matrix of the device terminated with a short-circuited gate, $S^{sh'}$. In this case, $S_{12}^{sh'}$=0 (so that the term on g_{11} vanishes) and $S_{22}^{sh'}$=S_{22}-$S_{12}S_{21}$/(1+S_{11}), see eq. (3), thus providing the responsivity with short-circuited gate $\beta_d^{CFsh}(f)$ as:

$$\beta_d^{CFsh}(f)=\frac{R_0}{2}g_{02}\left|1+S_{22}^{sh'}\right|^2=\frac{R_0}{2}g_{02}\left|1+S_{22}-\frac{S_{12}S_{21}}{1+S_{11}}\right|^2. \tag{8}$$

Figs. 5(b) and (c) show a very good agreement in the low frequency region (below 1 THz, approximately) between the MC results and the values of $\beta_d^{CFsh}(f)$.

Another very significant conclusion of this comparison is that, even if eq. (6) predicts an important enhancement of the responsivity at THz frequencies due to plasma effects, direct MC simulations show that it is very small, and the expected resonant plasma detection almost vanishes (even if a slight increase is observed in the 4-5 THz range, surprisingly taking positive values). These results also indicate that the resistive self-mixing mechanism described by the closed-form expression of eq. (6) appears to be at the origin of the detection at frequencies even approaching 1 THz, while plasma/thermoemission effects, clearly visible in the Y parameters of Fig. 3, have a significant influence at frequencies above that range. We attribute the discrepancy between the MC results and the prediction of the closed-form expression to the assumption of real and frequency-independent values of the g_{ij} coefficients. The frequency dependent nonlinearity and the possible phase shift between the voltage excitation and the current response should be taken into account in the model through complex frequency dependent g_{ij} coefficients.

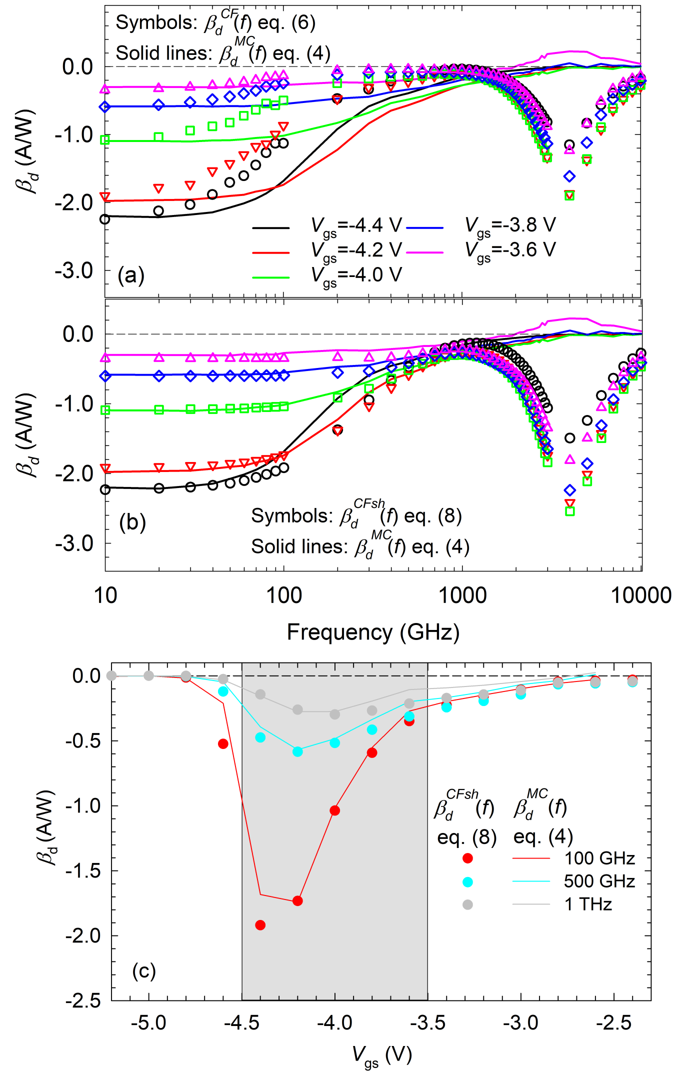

Fig. 5. Comparison of the current responsivity in (A/W) for different V_{gs} computed directly with MC simulations and eq. (4), $\beta_d^{MC}(f)$ (lines), with the predictions of the analytical CF models (symbols) of eq. (6), $\beta_d^{CF}(f)$ in (a) and eq. (8), $\beta_d^{CFsh}(f)$ in (b). In (c), the comparison between $\beta_d^{MC}(f)$ and $\beta_d^{CFsh}(f)$ is performed as a function of V_{gs} for different frequencies.

IV. Conclusion

We have performed MC simulations of AC power detection by AlGaN/GaN HEMTs in drain injection configuration. The simulator has been calibrated by comparison with measurements, achieving a very good fitting of the output characteristics of a 150 nm-gate transistor with 2×25 μm width. Direct MC calculations of the zero-bias drain current responsivity of the device to AC power reaching the THz range $\beta_d(f)$ have been compared to an estimation obtained by means of a close-form model based on a second-order Taylor series expansion of the output current, with static coefficients calculated from the DC curves and the frequency dependence included by means of the S-parameters (obtained from the MC simulation of the Y-parameters). This last approach allows identifying the direct-drain and drain-gate coupling contributions to the responsivity and its frequency dependence.

The agreement between the direct MC calculation of the responsivity and the Taylor-based estimation using constant g_{ij} coefficients is remarkable up to frequencies reaching 1 THz. At frequencies beyond that range, the calculated Y and S parameters exhibit plasma resonances which, been present in the values of $\beta_d^{CF}(f)$ estimated with the closed-form model, do not appear in the direct MC calculations $\beta_d^{MC}(f)$, what

indicates that the static approach used for the calculation of the Taylor coefficients is not valid at such high frequencies.

References

[1] S. S. Dhillon, M. S. Vitiello, E. H. Linfield, A. G. Davies, M. C. Hoffmann, J. Booske, C. Paoloni, M. Gensch, P. Weightman, G. P. Williams, E. Castro-Camus, D. R. S. Cumming, F. Simoens, I. Escorcia-Carranza, J. Grant, S. Lucyszyn, M. Kuwata-Gonokami, K. Konishi, M. Koch, C. A. Schmuttenmaer, T. L. Cocker, R. Huber, A. G. Markelz, Z. D. Taylor, V. P. Wallace, J. A. Zeitler, J. Sibik, T. M. Korter, B. Ellison, S. Rea, P. Goldsmith, K. B. Cooper, R. Appleby, D. Pardo, P. G. Huggard, V. Krozer, H. Shams, M. Fice, C. Renaud, A. Seeds, A. Stöhr, M. Naftaly, N. Ridler, R. Clarke, J. E. Cunningham, and M. B. Johnston, "The 2017 terahertz science and technology roadmap," *Journal of Physics D: Applied Physics*, vol. 50, no. 4, p. 043001, jan 2017.

[2] F. Sizov and A. Rogalski, "THz detectors," *Progress in Quantum Electronics*, vol. 34, no. 5, pp. 278–347, 2010.

[3] E. Javadi, D. B. But, K. Ikamas, J. Zdanevičius, W. Knap, and A. Lisauskas, "Sensitivity of field-effect transistor-based terahertz detectors," *Sensors*, vol. 21, no. 9, 2021.

[4] [Online]. Available: https://www.vadiodes.com/en/products/detectors

[5] M. A. Andersson and J. Stake, "An accurate empirical model based on volterra series for fet power detectors," *IEEE Transactions on Microwave Theory and Techniques*, vol. 64, no. 5, pp. 1431–1441, 2016.

[6] X. Yang, A. Vorobiev, K. Jeppson, and J. Stake, "Describing broadband terahertz response of graphene FET detectors by a classical model," *IEEE Transactions on Terahertz Science and Technology*, vol. 10, no. 2, pp. 158–166, 2020.

[7] M. Bauer, A. Rämer, S. A. Chevtchenko, K. Y. Osipov, D. Čibiraitė, S. Pralgauskaitė, K. Ikamas, A. Lisauskas, W. Heinrich, V. Krozer, and H. G. Roskos, "A high-sensitivity AlGaN/GaN HEMT terahertz detector with integrated broadband bow-tie antenna," *IEEE Transactions on Terahertz Science and Technology*, vol. 9, no. 4, pp. 430–444, 2019.

[8] A. Lisauskas, U. Pfeiffer, E. Öjefors, P. H. Bolìvar, D. Glaab, and H. G. Roskos, "Rational design of high-responsivity detectors of terahertz radiation based on distributed self-mixing in silicon field-effect transistors," *Journal of Applied Physics*, vol. 105, no. 11, p. 114511, 06 2009.

[9] W. Knap, F. Teppe, Y. Meziani, N. Dyakonova, J. Lusakowski, F. Boeuf, T. Skotnicki, D. Maude, S. Rumyantsev, and M. S. Shur, "Plasma wave detection of sub-terahertz and terahertz radiation by silicon field-effect transistors," *Applied Physics Letters*, vol. 85, no. 4, pp. 675–677, 07 2004.

[10] J. Marczewski, D. Tomaszewski, M. Zaborowski, and P. Bajurko, "Thermoemission-based model of THz detection and its validation—JLFET case studies," *IEEE Transactions on Terahertz Science and Technology*, vol. 12, no. 6, pp. 633–647, 2022.

[11] H. Hou, Z. Liu, J. Teng, T. Palacios, and S.-J. Chua, "A sub-terahertz broadband detector based on a GaN high-electron-mobility transistor with nanoantennas," *Applied Physics Express*, vol. 10, no. 1, p. 014101, nov 2016.

[12] J. Mateos and T. Gonzalez, "Plasma enhanced terahertz rectification and noise in InGaAs HEMTs," *IEEE Transactions on Terahertz Science and Technology*, vol. 2, no. 5, pp. 562–569, 2012.

[13] G. Paz-Martínez, P. Artillan, J. Mateos, E. Rochefeuille, T. González, and I. Íñiguez-de-la Torre, "A closed-form expression for the frequency-dependent microwave responsivity of transistors based on the I–V curve and S-Parameters," *IEEE Transactions on Microwave Theory and Techniques*, vol. 72, no. 1, pp. 415–420, 2024.

[14] C. Jacoboni and P. Lugli, *The Monte Carlo method for semiconductor device simulation*. Springer-Verlag, 1989.

[15] S. García, S. Pérez, I. Íñiguez-De-La-Torre, J. Mateos, and T. González, "Comparative Monte Carlo analysis of InP-and GaN-based Gunn diodes," *Journal of Applied Physics*, vol. 115, no. 044510, 2014.

[16] H. Sánchez-Martín, I. Íñiguez-de-la Torre, S. García-Sánchez, J. Mateos, and T. González, "Monte carlo analysis of thermal effects in the DC and AC performance of AlGaN/GaN HEMTs," *Solid-State Electronics*, vol. 193, p. 108289, 2022.

[17] W. H. Press, *The art of scientific computing*. Cambridge university press, 1992.

[18] J. Mateos, T. Gonzalez, D. Pardo, V. Hoel, H. Happy, and A. Cappy, "Improved monte carlo algorithm for the simulation of /spl delta/-doped alinas/gainas hemts," *IEEE Transactions on Electron Devices*, vol. 47, no. 1, pp. 250–253, 2000.

[19] T. González and D. Pardo, "Physical models of ohmic contact for monte carlo device simulation," *Solid-State Electronics*, vol. 39, no. 4, pp. 555–562, 1996.

[20] J. Mateos, T. González, D. Pardo, V. Hoel, and A. Cappy, "Effect of the T-gate on the performance of recessed hemts. a Monte Carlo analysis," *Semiconductor Science and Technology*, vol. 14, no. 9, p. 864, sep 1999.

[21] J. Mateos, T. González, D. Pardo, P. Tadyszak, F. Danneville, and A. Cappy, "Noise and transit time in ungated FET structures," *IEEE Transactions on Electron Devices*, vol. 44, no. 12, pp. 2128–2135, 1997.

[22] S. García Sánchez, "Monte carlo analysis of gunn oscillations and thermal effects in GaN-based devices," Ph.D. dissertation, Facultad de Ciencias, Universidad de Salamanca. [Online]. Available: http://dx.doi.org/10.14201/gredos.129407

[23] O. Madelung, *Semiconductors: data handbook*. Springer Science & Business Media, 2004.

[24] J. Mateos, T. González, D. Pardo, V. Hoël, and A. Cappy, "Monte carlo simulator for the design optimization of low-noise HEMTs," *IEEE Transactions on Electron Devices*, vol. 47, no. 10, pp. 1950–1956, 2000.

[25] H. Rodilla, T. González, D. Pardo, and J. Mateos, "High-mobility heterostructures based on InAs and InSb: A Monte Carlo study," *Journal of Applied Physics*, vol. 105, no. 11, 2009.

[26] S. García, I. Íñiguez-de-la Torre, O. García-Pérez, J. Mateos, T. González, P. Sangaré, C. Gaquière, and S. Pérez, "Self-consistent electro-thermal simulations of AlGaN/GaN diodes by means of Monte Carlo method," *Semiconductor Science and Technology*, vol. 30, no. 3, p. 035001, jan 2015.

[27] G. Paz-Martínez, I. Íñiguez-de-la Torre, H. Sánchez-Martín, T. González, and J. Mateos, "Analysis of GaN-Based HEMTs operating as RF detectors over a wide temperature range," *IEEE Transactions on Microwave Theory and Techniques*, vol. 71, no. 7, pp. 3126–3135, 2023.

[28] S. Rennesson, F. Lecourt, N. Defrance, M. Chmielowska, S. Chenot, M. Lesecq, V. Hoel, E. Okada, Y. Cordier, and J.-C. De Jaeger, "Optimization of $Al_{0.29}Ga_{0.71}N$/GaN high electron mobility heterostructures for high-power/frequency performances," *IEEE Transactions on Electron Devices*, vol. 60, no. 10, pp. 3105–3111, 2013.

[29] P. Asbeck, E. Yu, S. Lau, G. Sullivan, J. Van Hove, and J. Redwing, "Piezoelectric charge densities in AlGaN/GaN HFETs," *Electronics letters*, vol. 33, no. 14, pp. 1230–1231, 1997.

[30] E. Yu, X. Dang, P. Asbeck, S. Lau, and G. Sullivan, "Spontaneous and piezoelectric polarization effects in III-V nitride heterostructures," *Journal of Vacuum Science & Technology B: Microelectronics and Nanometer Structures Processing, Measurement, and Phenomena*, vol. 17, no. 4, pp. 1742–1749, 1999.

[31] V. Fiorentini, F. Bernardini, and O. Ambacher, "Evidence for nonlinear macroscopic polarization in III-V nitride alloy heterostructures," *Applied physics letters*, vol. 80, no. 7, pp. 1204–1206, 2002.

[32] S. Babiker, A. Asenov, N. Cameron, and S. Beaumont, "Simple approach to include external resistances in the Monte Carlo simulation of MESFETs and HEMTs," *IEEE Transactions on Electron Devices*, vol. 43, no. 11, pp. 2032–2034, 1996.

[33] R. Bauer and P. Penfield, "De-Embedding and Unterminating," *IEEE Transactions on Microwave Theory and Techniques*, vol. 22, no. 3, pp. 282–288, 1974.

[34] D. Frickey, "Conversions between S, Z, Y, H, ABCD, and T parameters which are valid for complex source and load impedances," *IEEE Transactions on Microwave Theory and Techniques*, vol. 42, no. 2, pp. 205–211, 1994.